On-Demand Integrated Quantum Memory for Polarization Qubits

Tian-Xiang Zhu,[1,2,3] Chao Liu,[1,2,3] Ming Jin,[1,2,3] Ming-Xu Su,[1,2,3] Yu-Ping Liu,[1,2,3] Wen-Juan Li,[4] Yang Ye,[4] Zong-Quan Zhou,[1,2,3,*] Chuan-Feng Li,[1,2,3,†] and Guang-Can Guo[1,2,3]

[1]*CAS Key Laboratory of Quantum Information, University of Science and Technology of China, Hefei 230026, China*

[2]*CAS Center for Excellence in Quantum Information and Quantum Physics, University of Science and Technology of China, Hefei, 230026, China*

[3]*Hefei National Laboratory, Hefei 230088, China*

[4]*Center for Micro and Nanoscale Research and Fabrication, University of Science and Technology of China, Hefei 230026, China*

(Received 12 February 2022; accepted 28 March 2022; published 2 May 2022)

Photonic polarization qubits are widely used in quantum computation and quantum communication due to the robustness in transmission and the easy qubit manipulation. An integrated quantum memory for polarization qubits is a useful building block for large-scale integrated quantum networks. However, on-demand storing polarization qubits in an integrated quantum memory is a long-standing challenge due to the anisotropic absorption of solids and the polarization-dependent features of microstructures. Here we demonstrate a reliable on-demand quantum memory for polarization qubits, using a depressed-cladding waveguide fabricated in a $^{151}Eu^{3+}:Y_2SiO_5$ crystal. The site-2 $^{151}Eu^{3+}$ ions in Y_2SiO_5 crystal provides a near-uniform absorption for arbitrary polarization states and a new pump sequence is developed to prepare a wideband and enhanced absorption profile. A fidelity of $99.4 \pm 0.6\%$ is obtained for the qubit storage process with an input of 0.32 photons per pulse, together with a storage bandwidth of 10 MHz. This reliable integrated quantum memory for polarization qubits reveals the potential for use in the construction of integrated quantum networks.

DOI: 10.1103/PhysRevLett.128.180501

Quantum memories (QMs) are fundamental building blocks for global-scale quantum networks [1]. Integrated QMs are particularly useful to meet the requirements of convenience and miniaturization in large-scale applications [2]. QMs have been implemented in various physical systems such as single atoms [3], single ions [4], cold atoms [5,6], warm atomic vapors [7,8], defects in solids [9,10] and rare-earth-ion doped crystals (REICs) [2,11]. As a solid-state platform, REICs have extremely long storage times [12–15], large bandwidth [2,16–19], large multimode capacities [13,18,20–26], and can be easily manufactured to be integrated QMs [2,16,17,26–32].

As the natural carrier of information in quantum networks, photonic qubits can be coded into various degrees of freedom, such as polarization, time, path, and frequency. Among them, the polarization qubits are widely adopted due to the easy manipulation with wave plates and easy transmission in a single temporal and spatial mode. QMs for photonic polarization qubits have been demonstrated in REICs [33–37], single atoms [3], cold atomic ensembles [5,38,39], and warm atomic vapors [40]. However, on-demand integrated QMs for polarization qubits have not yet been achieved. There are two problems that need to be solved. First, unlike free-space atoms [3], most solids have anisotropic absorption. For REICs, pioneering works solved this problem by storing two different polarization components into spatially different parts of the medium [33–35,37]. Such an approach is not suitable for integrated QMs due to the complex optical setup which may introduce unwanted losses. An amorphous glass fiber can provide a uniform absorption [36] at a price of much less storage time as compared to that of single-crystal hosts. Second, to date, all integrated QMs fabricated on REICs are polarization dependent [2,12,17,26–32,41–51], i.e., only one polarization mode is supported in these micro- and nanostructures.

Here, we demonstrate an integrated QM for polarization qubits by fabricating polarization-independent waveguides in a uniformly absorbing single crystal. The depressed-cladding optical waveguide, also known as the type-III waveguide [52], is fabricated using femtosecond laser micromachining (FLM). This optical waveguide is further combined with on-chip electrodes to facilitate on-demand retrieval in discrete steps based on the Stark-modulated atomic frequency comb protocol [31,53,54].

The substrate is a 0.1% doped $^{151}Eu^{3+}:Y_2SiO_5$ crystal with a size of $3 \times 12 \times 4$ mm^3 along $D1 \times D2 \times b$ axes. The type-III waveguide is fabricated by a FLM system (WOPhotonics). The details of the fabrication process are provided in the Supplemental Material [55]. In the type-III waveguide, the low refractive-index optical barriers are separated by a few microns and the optical field is confined among them [52,56]. To achieve a near-uniform absorption

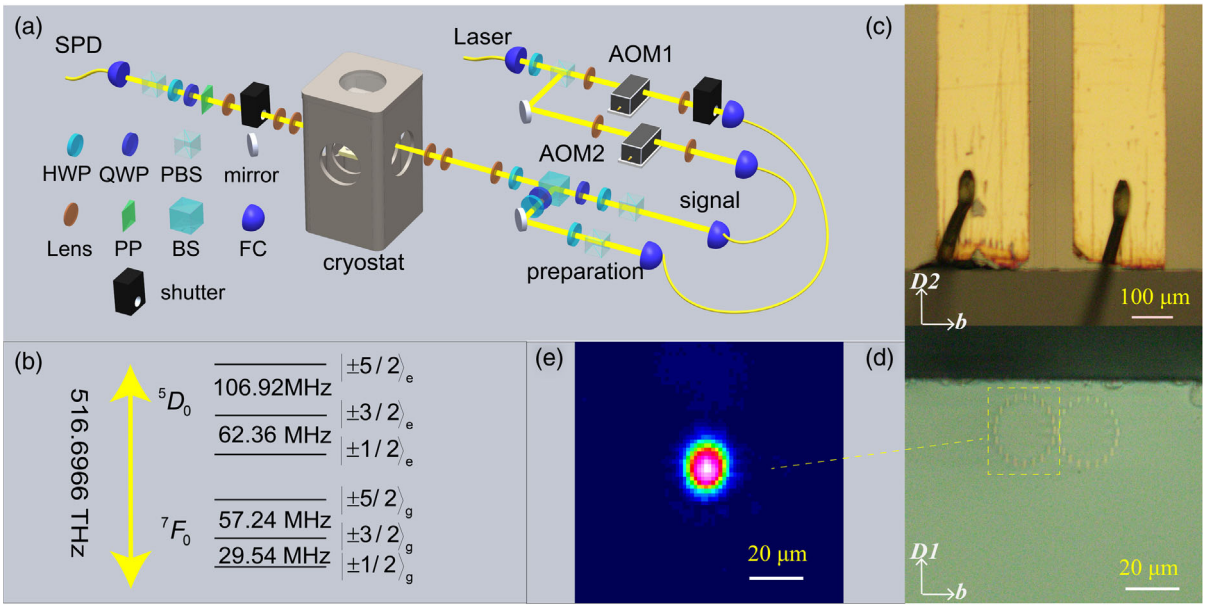

FIG. 1. Experimental setup. (a) Schematic of the setup. The signal and the preparation beams generated by the acousto-optic modulation in double-pass configurations are combined by a beam splitter (BS) and coupled into the type-III waveguide by lens group. The polarization of the signal qubits is prepared by a polarization beam splitter (PBS), a half wave plate (HWP), and a quarter-wave plate (QWP). The HWP after the BS is employed to match the axial direction of the crystal. Another lens group is used for collecting the emergent light from the waveguide. A phase plate (PP) is used to compensate the phase difference between the TE and TM modes because of waveguide birefringence and the phase difference accumulated in the setup. The polarization of signal photons is analyzed using a QWP, HWP, and BS. The signal is finally coupled into a fiber coupler (FC) and detected by a single photon detector (SPD). (b) Energy diagram of transition for site-2 $^{151}Eu^{3+}$ ions in $^{151}Eu^{3+}:Y_2SiO_5$ at zero magnetic field [58]. (c) The vertical view of type-III waveguides and the electrodes with a scale bar is 100 μm. (d) The front view of the two type-III waveguides with a scale bar is 20 μm. The left waveguide is the one used in the experiment, which has a lower insertion loss as compared to the right one. (e) The beam profile of the TM mode at the exit of the waveguide as measured by a charge coupled device with a scale bar is 20 μm.

for arbitrary polarization states, we use ions that locate at site-2 of Y_2SiO_5 crystals and the light propagates along the $D2$ direction [57,58].

The TM (TE) guide mode is single mode and its polarization direction matches the $D1$ (b) axis. The mode intensity profiles of TM and TE modes are almost the same. As shown in Fig. 1(e), the full width at half-maximum (FWHM) of the TM mode is 9.0 μm × 10.3 μm ($D1 \times b$). For convenience, we denote the polarization state parallel to the $D1$ (b) axis as $|H\rangle$ ($|V\rangle$). The insertion losses (including coupling losses and propagation losses) are 0.85 (0.84) dB for $|H\rangle$ ($|V\rangle$) and the coupling efficiency of the output mode to a single-mode fiber (SMF) is approximately 80%. The optical waveguide is fabricated at a depth of 20 μm beneath the surface of the crystal for efficient interface with the on-chip electrodes. The two parallel electrodes have a width of 200 μm and a spacing of 100 μm. An arbitrary function generator (Tektronix, AFG3102C) is employed to directly drive the electrodes to introduce the required electric field on the $^{151}Eu^{3+}$ ions inside the optical waveguide.

The schematic drawing of the experimental setup is presented Fig. 1(a). The 580-nm laser is a frequency-doubled semiconductor laser with a stabilized linewidth of below 1 kHz. Both the signal beam and the preparation beam are controlled by acousto-optic modulators (AOMs) which are driven by arbitrary waveform generators. These two beams are combined into a single beam and coupled into the waveguide memory which is cooled down to 3.4 K using a cryostat (Montana Instruments). The polarization state of the signal is prepared and analyzed with standard wave plates and polarization beam splitters. The signal beam is decreased to single-photon levels and two shutters are employed to protect the single photon detectors from the strong preparation beam.

An atomic frequency comb (AFC) is a well-established quantum storage protocol in REICs with the advantages of large bandwidth [2,16,18,19], high fidelity [11,21,33–35], and excellent multimode capability [13,18,20–26]. The recently proposed Stark-modulated atomic frequency comb (SMAFC) protocol [31,53,54] could further enable on-demand readout in discrete steps by employing electric field pulses to actively control the rephasing process of an AFC.

In Y_2SiO_5 crystals, when the electric fields are parallel to the b axis or in the mirror plane, the doped ions will be split into two groups by the Stark effect [31,53,54]. These two groups of ions have frequency shifts of the equal amounts

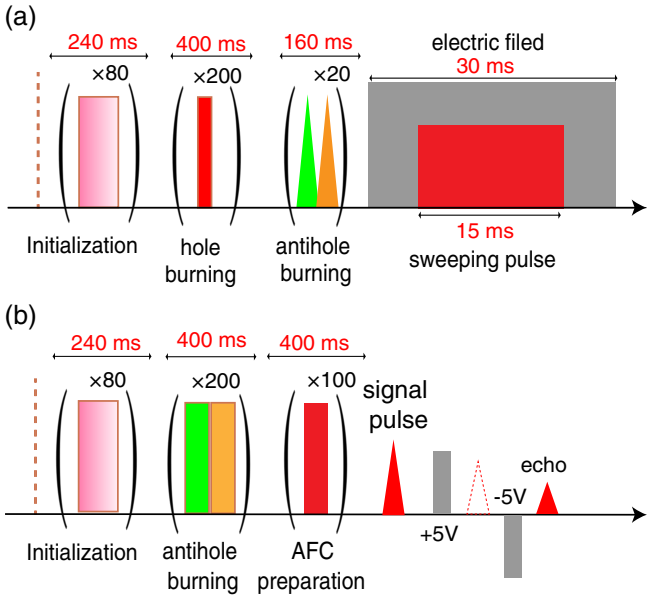

FIG. 2. (a) Time sequence for the measurement of the linear Stark splitting. After preparation of the antihole, the spectral feature is measured with sweeping optical pulse with applied electric fields. (b) Time sequence for SMAFC storage. After preparation of AFC, two electric pulse actively control the readout times of the echo. The standard AFC echo is suppressed by the first electric pulse and the SMAFC echo is retrieved after the second electric pulse.

but with opposite directions. The linear Stark splitting of the $^{151}Eu^{3+}$ ions at two crystalline sites in Y_2SiO_5 crystals has been measured when the electric fields are parallel to the $D1$ and $D2$ axes [59]. Here, we further characterize the Stark splitting of site-2 Eu^{3+} ions when the electric field is parallel to the b axis.

The Stark splittings are measured by spectral-hole burning spectroscopy [31,59]. Under a biased electric field along with the b axis, an antihole will split into two antiholes. The linear Stark splitting along the b axis of site-2 $^{151}Eu^{3+}$ are 5.66 ± 0.03 KHz/$(\mathrm{V}\cdot\mathrm{cm}^{-1})$ and -5.71 ± 0.04 KHz/$(\mathrm{V}\cdot\mathrm{cm}^{-1})$ with the average value 5.69 ± 0.04 KHz/$(\mathrm{V}\cdot\mathrm{cm}^{-1})$. Time sequence for the measurement is presented in Fig. 2(a) and more details are provided in the Supplemental Material [55].

Then we continue our experiment with on-demand storage based on SMAFC. Considering combs with Gaussian profiles, the storage efficiency of the SMAFC memory [53] is

$$\eta(t) = \frac{\pi}{4\ln(2)}(d/F)^2 e^{\left(-\sqrt{\frac{\pi}{4\ln(2)}}d/F\right)} e^{\left(-\frac{\pi^2}{2\ln(2)}t^2\gamma^2\right)}, \quad (1)$$

where d is the absorption depth, F is the finesse of the comb, γ is the comb FWHM, and t is the storage time. It is obvious that high finesse (F) and high absorption depth (d) are extremely important for achieving high efficiency storage. However, the $^7F_0 \rightarrow {}^5D_0$ transition of Eu^{3+} is only weakly allowed in Y_2SiO_5 crystals and this problem is even worse when working with site-2 Eu^{3+} ions [57]. In our experiment, the natural sample absorption $d = 1.46$ (1.64) for $|H\rangle$ ($|V\rangle$). A preparation process is employed to enhance the effective absorption depth by increasing the population that can be excited in the target frequency range. The time sequence for this experiment is presented in Fig. 2(b) and more details are provided in the Supplemental Material [55]. Successively utilizing the pump light at the center frequency of $f_0 + 33.02$ MHz and $f_0 - 33.02$ MHz with the chirping bandwidth of 46 MHz, we prepare a 12.68-MHz enhanced absorption peak at the center frequency of f_0. Using our optical pumping scheme, the enhanced d is 3.85 (4.35) for $|H\rangle$ ($|V\rangle$) with the average magnitude of enhancement of 2.64 times as compared to the original absorption.

Next, we create an AFC structure with a comb spacing of 2 MHz and a total bandwidth of 10 MHz by parallel comb preparation scheme [60]. The comb structures are shown in Figs. 3(a) and 3(b) for input light of two orthogonal polarization states. Our AFC is an imperfect square comb and the expected AFC storage efficiency is between that can be obtained with the Gaussian comb [Eq. (1)] and the square comb [60]. The measured efficiencies of the 500-ns AFC are $23.3 \pm 0.3\%$ ($26.9 \pm 0.3\%$) for $|H\rangle$ ($|V\rangle$). The theoretical efficiencies are 29.6% (32.0%) for $|H\rangle$ ($|V\rangle$) for the square-comb model and 21.5% (24.2%) for the Gaussian-comb model.

The simple two-level AFC only allows predetermined storage times. To actively control the AFC rephasing process, we further applied electric field pulses to implement a SMAFC. The first electric pulse with a duration of 85 ns and a voltage of 5 V is applied before the first AFC echo, to prevent the emission of 1st to $(n-1)$th order AFC echoes. Then the second pulse with reversed polarity is applied before the nth order AFC echo, so that to compensate the Stark-induced phase and readout the nth order AFC echo in an on-demand fashion. Photon counting histograms for input states of $|H\rangle$ ($|V\rangle$) are presented in Figs. 3(c) and 3(d), respectively. The input pulses contain 0.32 photons on average in the input side of the cryostat. The internal storage efficiencies of the 1-μs SMAFC echo are $13.2 \pm 0.8\%$ and $15.5 \pm 0.8\%$ for $|H\rangle$ and $|V\rangle$, respectively. Since the efficiencies of other optical components, such as the single-mode fiber coupling, also have slight polarization dependence, the device efficiencies (between the input of the cryostat and the detector) for 1-μs SMAFC storage are $7.0 \pm 0.4\%$ and $7.6 \pm 0.4\%$ for $|H\rangle$ and $|V\rangle$, respectively, which is approximately balanced for storage of arbitrary polarization states [Fig. 3(e)].

For 1-μs SMAFC storage, with an average photon number of 0.32 photons per input pulse, the measured signal to noise ratios (SNRs) are 1265 ± 729 and 1039 ± 520 for $|H\rangle$ ($|V\rangle$), respectively. Here, the SNR is defined by

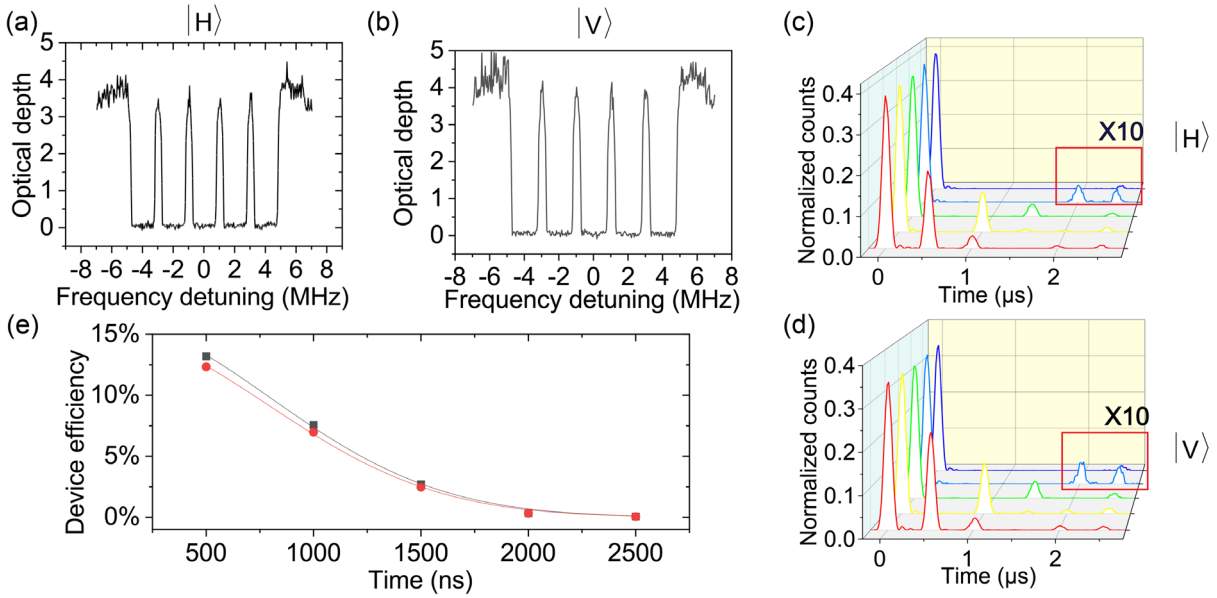

FIG. 3. SMAFC memory for weak coherent pulses. Figures 1(a) and 1(b) are the measured comb structures with input states of $|H\rangle$ and $|V\rangle$, respectively. The average peak absorption depth is 3.6 (4.0) for $|H\rangle$ ($|V\rangle$) with negligible background absorption. Figs. 1(c) and 1(d) are photon counting histograms for SMAFC storage, with input states of $|H\rangle$ and $|V\rangle$, respectively. Echoes retrieved after 2 s are magnified by 10 times. (e) The device efficiency of the SMAFC memory for input states of $|H\rangle$ (red) and $|V\rangle$ (black). The fitted γ is 335 ± 6 kHz (333 ± 7 kHz) for $|H\rangle$ ($|V\rangle$), according to Eq. (1).

$(S-N)/N$, where S (N) is the photon counts at output window with (without) input pulses. Such a high SNR could allow high-fidelity polarization qubit storage. Quantum process tomography is performed to benchmark the performance of the qubit storage of our device [35,61]. The fidelities of retrieved states are $99.9\% \pm 0.1\%$, $99.8\% \pm 0.1\%$, $99.9\% \pm 0.1\%$, and $98.4\% \pm 1.4\%$ for input states of $|H\rangle$, $|V\rangle$, $|H + iV\rangle$, and $|H + V\rangle$, respectively. The process matrix is constructed based on the maximum likelihood estimation, with a fidelity of $99.4 \pm 0.6\%$ to the ideal identical storage process (Fig. 4). Here the error bar refers to one standard deviation given by the Monte Carlo simulation assuming the Poisson statistics of photons. Taking into account the finite storage efficiency of 7.0% and the Poisson statistics of the weak coherent pulse, the maximal achievable fidelity using a classical measure and prepare strategy is 76.2% [25]. Our result outperforms such strict classical bound by 39 standard deviations, unambiguously demonstrating that this device operates in the quantum regime.

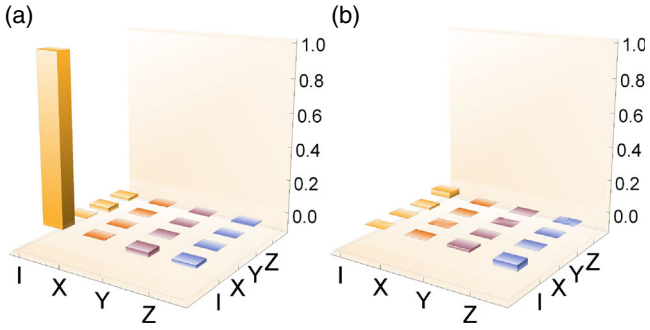

FIG. 4. The reconstructed process matrix of the storage process. (a) The real part of the process matrix as obtained by the quantum process tomography [61]. The horizontal axes are the basis operators in the two-dimensional Hilbert space. (b) The imaginary part of the process matrix with the largest imaginary element of 0.035.

In conclusion, we fabricate a depressed-cladding optical waveguide and on-chip electrodes in a $^{151}Eu^{3+}:Y_2SiO_5$ crystal. On-demand storage of polarization qubits with a bandwidth of 10 MHz is achieved by implementing a SMAFC protocol using site-2 Eu^{3+} ions. The fidelity of the storage process reaches $99.4 \pm 0.6\%$, which is approximately the same as that achieved with the bulk material [34] but provides the additional capability of on-demand retrieval.

The unique advantage of the current integrated QM is the capability of supporting arbitrary polarization which could play an essential role in quantum networks involving polarization qubits. A further extension of the current work would be the implementation of spin-wave storage protocols [62,63] which can provide an extended storage time of up to 1 h using the current material [15]. As compared to the SMAFC, spin-wave memories can provide on-demand retrieval in a continuous fashion and much longer storage times. However, elimination of noise would be much more challenging since strong control pulses are required during the storage process. For spin-wave storage, our device could further provide high-contrast polarization filtering of

strong control pulses which copropagate with a single-photon signal field in the same waveguide. Moreover, such integrated structure could enable high-density spatial-multiplexed storage for transportable quantum memories [15,64] and quantum repeaters [1,18] which are viable solutions for long-distance quantum communication.

This work is supported by the National Key R&D Program of China (No. 2017YF A0304100), Innovation Program for Quantum Science and Technology (No. 2021ZD0301200), the National Natural Science Foundation of China (No. 11774331, No. 11774335, No. 11821404, and No. 11654002), the Fundamental Research Funds for the Central Universities (No. WK2470000026 and No. WK2470000029) and this work was partially carried out at the USTC Center for Micro and Nanoscale Research and Fabrication. Z.-Q. Z. acknowledges the support from the Youth Innovation Promotion Association CAS.

*zq_zhou@ustc.edu.cn
†cfli@ustc.edu.cn

[1] N. Sangouard, C. Simon, H. de Riedmatten, and N. Gisin, Rev. Mod. Phys. **83**, 33 (2011).
[2] E. Saglamyurek, N. Sinclair, J. Jin, J. A. Slater, D. Oblak, F. Bussieres, M. George, R. Ricken, W. Sohler, and W. Tittel, Nature (London) **469**, 512 (2011).
[3] H. P. Specht, C. Nlleke, A. Reiserer, M. Uphoff, E. Figueroa, S. Ritter, and G. Rempe, Nature (London) **473**, 190 (2011).
[4] D. L. Moehring, P. Maunz, S. Olmschenk, K. C. Younge, D. N. Matsukevich, L.-M. Duan, and C. Monroe, Nature (London) **449**, 68 (2007).
[5] K. S. Choi, H. Deng, J. Laurat, and H. Kimble, Nature (London) **452**, 67 (2008).
[6] Y. Yu, F. Ma, X.-Y. Luo, B. Jing, P.-F. Sun, R.-Z. Fang, C.-W. Yang, H. Liu, M.-Y. Zheng, and X.-P. Xie, Nature (London) **578**, 240 (2020).
[7] J. Appel, E. Figueroa, D. Korystov, M. Lobino, and A. I. Lvovsky, Phys. Rev. Lett. **100**, 093602 (2008).
[8] M. Hosseini, B. M. Sparkes, G. Campbell, P. K. Lam, and B. C. Buchler, Nat. Commun. **2**, 174 (2011).
[9] G. D. Fuchs, G. Burkard, P. V. Klimov, and D. D. Awschalom, Nat. Phys. **7**, 789 (2011).
[10] B. Hensen, H. Bernien, A. E. Drau, A. Reiserer, N. Kalb, M. S. Blok, J. Ruitenberg, R. F. Vermeulen, R. N. Schouten, and C. Abelln, Nature (London) **526**, 682 (2015).
[11] H. de Riedmatten, M. Afzelius, M. U. Staudt, C. Simon, and N. Gisin, Nature (London) **456**, 773 (2008).
[12] M. Zhong, M. P. Hedges, R. L. Ahlefeldt, J. G. Bartholomew, S. E. Beavan, S. M. Wittig, J. J. Longdell, and M. J. Sellars, Nature (London) **517**, 177 (2015).
[13] C. Laplane, P. Jobez, J. Etesse, N. Gisin, and M. Afzelius, Phys. Rev. Lett. **118**, 210501 (2017).
[14] M. Rani, M. P. Hedges, R. L. Ahlefeldt, and M. J. Sellars, Nat. Phys. **14**, 50 (2018).
[15] Y. Ma, Y.-Z. Ma, Z.-Q. Zhou, C.-F. Li, and G.-C. Guo, Nat. Commun. **12**, 2381 (2021).
[16] E. Saglamyurek, M. Grimau Puigibert, Q. Zhou, L. Giner, F. Marsili, V. B. Verma, S. Woo Nam, L. Oesterling, D. Nippa, D. Oblak, and W. Tittel, Nat. Commun. **7**, 11202 (2016).
[17] T. Zhong, J. M. Kindem, J. Rochman, and A. Faraon, Nat. Commun. **8**, 14107 (2017).
[18] X. Liu, J. Hu, Z.-F. Li, X. Li, P.-Y. Li, P.-J. Liang, Z.-Q. Zhou, C.-F. Li, and G.-C. Guo, Nature (London) **594**, 41 (2021).
[19] I. Usmani, M. Afzelius, H. de Riedmatten, and N. Gisin, Nat. Commun. **1**, 12 (2010).
[20] N. Sinclair, E. Saglamyurek, H. Mallahzadeh, J. A. Slater, M. George, R. Ricken, M. P. Hedges, D. Oblak, C. Simon, W. Sohler, and W. Tittel, Phys. Rev. Lett. **113**, 053603 (2014).
[21] Z.-Q. Zhou, Y.-L. Hua, X. Liu, G. Chen, J.-S. Xu, Y.-J. Han, C.-F. Li, and G.-C. Guo, Phys. Rev. Lett. **115**, 070502 (2015).
[22] J.-S. Tang, Z.-Q. Zhou, Y.-T. Wang, Y.-L. Li, X. Liu, Y.-L. Hua, Y. Zou, S. Wang, D.-Y. He, and G. Chen, Nat. Commun. **6**, 8652 (2015).
[23] K. Kutluer, M. Mazzera, and H. de Riedmatten, Phys. Rev. Lett. **118**, 210502 (2017).
[24] A. Seri, A. Lenhard, D. Rieländer, M. Gündoğan, P. M. Ledingham, M. Mazzera, and H. de Riedmatten, Phys. Rev. X **7**, 021028 (2017).
[25] T.-S. Yang, Z.-Q. Zhou, Y.-L. Hua, X. Liu, Z.-F. Li, P.-Y. Li, Y. Ma, C. Liu, P.-J. Liang, and X. Li, Nat. Commun. **9**, 3407 (2018).
[26] A. Seri, D. Lago-Rivera, A. Lenhard, G. Corrielli, R. Osellame, M. Mazzera, and H. de Riedmatten, Phys. Rev. Lett. **123**, 080502 (2019).
[27] E. Miyazono, T. Zhong, I. Craiciu, J. M. Kindem, and A. Faraon, Appl. Phys. Lett. **108**, 011111 (2016).
[28] T. Zhong, J. M. Kindem, J. G. Bartholomew, J. Rochman, I. Craiciu, E. Miyazono, M. Bettinelli, E. Cavalli, V. Verma, and S. W. Nam, Science **357**, 1392 (2017).
[29] A. Seri, G. Corrielli, D. Lago-Rivera, A. Lenhard, H. de Riedmatten, R. Osellame, and M. Mazzera, Optica **5**, 934 (2018).
[30] J. M. Kindem, A. Ruskuc, J. G. Bartholomew, J. Rochman, Y. Q. Huan, and A. Faraon, Nature (London) **580**, 201 (2020).
[31] C. Liu, T.-X. Zhu, M.-X. Su, Y.-Z. Ma, Z.-Q. Zhou, C.-F. Li, and G.-C. Guo, Phys. Rev. Lett. **125**, 260504 (2020).
[32] M. Raha, S. Chen, C. M. Phenicie, S. Ourari, A. M. Dibos, and J. D. Thompson, Nat. Commun. **11**, 1605 (2020).
[33] C. Clausen, F. Bussieres, M. Afzelius, and N. Gisin, Phys. Rev. Lett. **108**, 190503 (2012).
[34] M. Gündoğan, P. M. Ledingham, A. Almasi, M. Cristiani, and H. de Riedmatten, Phys. Rev. Lett. **108**, 190504 (2012).
[35] Z.-Q. Zhou, W.-B. Lin, M. Yang, C.-F. Li, and G.-C. Guo, Phys. Rev. Lett. **108**, 190505 (2012).
[36] J. Jin, E. Saglamyurek, Marcel. li Grimau Puigibert, V. Verma, F. Marsili, S. W. Nam, D. Oblak, and W. Tittel, Phys. Rev. Lett. **115**, 140501 (2015).
[37] C. Laplane, P. Jobez, J. Etesse, N. Timoney, N. Gisin, and M. Afzelius, New J. Phys. **18**, 013006 (2015).

[38] P. Vernaz-Gris, K. Huang, M. Cao, A. S. Sheremet, and J. Laurat, Nat. Commun. **9**, 363 (2018).
[39] Y. Wang, J. Li, S. Zhang, K. Su, Y. Zhou, K. Liao, S. Du, H. Yan, and S.-L. Zhu, Nat. Photonics **13**, 346 (2019).
[40] M. Namazi, C. Kupchak, B. Jordaan, R. Shahrokhshahi, and E. Figueroa, Phys. Rev. Applied **8**, 034023 (2017).
[41] G. Corrielli, A. Seri, M. Mazzera, R. Osellame, and H. de Riedmatten, Phys. Rev. Applied **5**, 054013 (2016).
[42] C. Liu, Z.-Q. Zhou, T.-X. Zhu, L. Zheng, M. Jin, X. Liu, P.-Y. Li, J.-Y. Huang, Y. Ma, and T. Tu, Optica **7**, 192 (2020).
[43] T.-X. Zhu, C. Liu, L. Zheng, Z.-Q. Zhou, C.-F. Li, and G.-C. Guo, Phys. Rev. Applied **14**, 054071 (2020).
[44] T. Zhong, J. M. Kindem, E. Miyazono, and A. Faraon, Nat. Commun. **6**, 8206 (2015).
[45] T. Zhong, J. Rochman, J. M. Kindem, E. Miyazono, and A. Faraon, Opt. Express **24**, 536 (2016).
[46] E. Miyazono, I. Craiciu, A. Arbabi, T. Zhong, and A. Faraon, Opt. Exp. **25**, 2863 (2017).
[47] T. Zhong, J. M. Kindem, J. G. Bartholomew, J. Rochman, I. Craiciu, V. Verma, S. W. Nam, F. Marsili, M. D. Shaw, A. D. Beyer, and A. Faraon, Phys. Rev. Lett. **121**, 183603 (2018).
[48] J. G. Bartholomew, J. Rochman, J. M. Kindem, A. Ruskuc, I. Craiciu, M. Lei, T. Zhong, and A. Faraon, in *2019 Conference on Lasers and Electro-Optics (CLEO)* (IEEE, San Jose, CA, 2019), pp. 1–2.
[49] I. Craiciu, M. Lei, J. Rochman, J. M. Kindem, J. G. Bartholomew, E. Miyazono, T. Zhong, N. Sinclair, and A. Faraon, Phys. Rev. Applied **12**, 024062 (2019).
[50] A. M. Dibos, M. Raha, C. M. Phenicie, and J. D. Thompson, Phys. Rev. Lett. **120**, 243601 (2018).
[51] S. Chen, M. Raha, C. M. Phenicie, S. Ourari, and J. D. Thompson, Science **370**, 592 (2020).
[52] F. Chen and J. V. de Aldana, Laser Photonics Rev. **8**, 251 (2014).
[53] S. P. Horvath, M. K. Alqedra, A. Kinos, A. Walther, J. M. Dahlström, S. Kröll, and L. Rippe, Phys. Rev. Research **3**, 023099 (2021).
[54] I. Craiciu, M. Lei, J. Rochman, J. G. Bartholomew, and A. Faraon, Optica **8**, 114 (2021).
[55] See Supplemental Material at http://link.aps.org/supplemental/10.1103/PhysRevLett.128.180501 for details about the experiment.
[56] N. Skryabin, A. Kalinkin, I. Dyakonov, and S. Kulik, Micromachines **11**, 1 (2020).
[57] F. Könz, Y. Sun, C. W. Thiel, R. L. Cone, R. W. Equall, R. L. Hutcheson, and R. M. Macfarlane, Phys. Rev. B **68**, 085109 (2003).
[58] M. Jin, Y.-Z. Ma, Z.-Q. Zhou, C.-F. Li, and G.-C. Guo, Sci. Bull. **67**, 676 (2022).
[59] S. Zhang, N. Lui, N. Galland, R. Le Targat, P. Goldner, B. Fang, S. Seidelin, and Y. Le Coq, Appl. Phys. Lett. **117**, 221102 (2020).
[60] P. Jobez, N. Timoney, C. Laplane, J. Etesse, A. Ferrier, P. Goldner, N. Gisin, and M. Afzelius, Phys. Rev. A **93**, 032327 (2016).
[61] J. L. O'Brien, G. J. Pryde, A. Gilchrist, D. F. V. James, N. K. Langford, T. C. Ralph, and A. G. White, Phys. Rev. Lett. **93**, 080502 (2004).
[62] Y.-Z. Ma, M. Jin, D.-L. Chen, Z.-Q. Zhou, C.-F. Li, and G.-C. Guo, Nat. Commun. **12**, 4378 (2021).
[63] M. Afzelius, C. Simon, H. de Riedmatten, and N. Gisin, Phys. Rev. A **79**, 052329 (2009).
[64] J. Bland-Hawthorn, M. J. Sellars, and J. G. Bartholomew, J. Opt. Soc. Am. B **38**, A86 (2021).